Hybrid potential model with high feasibility and flexibility for metallic and covalent solids

B. N. Yao,[1,2,3] Z. R. Liu,[1,2] D. Legut [4] and R. F. Zhang [1,2,*]

[1]*School of Materials Science and Engineering, Beihang University, Beijing 100191, People's Republic of China*

[2]*Center for Integrated Computational Materials Engineering (International Research Institute for Multidisciplinary Science) and Key Laboratory of High-Temperature Structural Materials & Coatings Technology (Ministry of Industry and Information Technology), Beihang University, Beijing 100191, People's Republic of China*

[3]*Shen Yuan Honors College, Beihang University, Beijing 100191, People's Republic of China*

[4]*IT4Innovations & Nanotechnology Center, CEET, VSB-Technical University of Ostrava, CZ-708 00 Ostrava, Czech Republic*

Pair-functional potentials are generally used for metallic solids, whereas cluster potentials are more appropriate for covalent solids; however, both face critical difficulties that cannot be solved based purely on the optimization of potential functions, e.g., the lattice stability for hcp metals with high *c/a* ratios and the conflict between stacking-fault energy and cleavage energy for covalent solids, which can be attributed to their respective physical foundations and approximations according to their bonding characteristics. By incorporating the long-range many-body effect in pair-functional potentials and the short-range angular-dependent terms in cluster potentials, a unified hybrid potential model is physically justified and proposed in the present study for both metallic and covalent bonding solids to resolve the aforementioned critical issues and other specific cases. The proposed model was not only successfully demonstrated for a series of elemental solids, including 20 fcc, bcc, and hcp metals and three covalent elements, but also was extended to construct cross potentials for three representative compound systems, i.e., CuNi, TiC, and BN, which suggests that the present hybrid potential model possess higher compatibility and feasibility for various metallic and covalent systems than the respective pair-functional potentials and cluster ones. Overall, the hybrid potential model not only complements the current potential library but also builds a foundation for further potential development with high flexibility.

I. INTRODUCTION

Materials genome engineering and integrated computational materials engineering have strategically established the fourth paradigm of materials research by incorporating the goal-oriented and mechanism-directed design [1], which necessitates high-throughput computations and simulations with high feasibility and confidence at different scales. Although the proposal of density-functional theory (DFT) with reliable pseudopotential has facilitated high-throughput first-principles calculations to derive various high-precision properties under ambient conditions, the deficiency of high-feasibility empirical interatomic potential still imposes limitations in the variety of material systems and the extension of transferability, specimen size, and simulation time for high-efficiency large-scale atomistic simulations under critical environments, e.g., defect interactions in crystals [2,3], plastic deformation mechanism [4–6], solid-state diffusion processes [7], phase competition [8], and crystal structure prediction [9], which fundamentally limits the applications in broad scenarios by considering the reliability and quality of the simulations.

The development of empirical potentials can be traced back to the pair potential [10], like the Lennard-Jones [11], Morse [12], and Born-Mayer models [13]; however, these models neglect the long-range many-body effects or short-range angular dependence, which inherently lead to certain drawbacks in deriving the properties of metallic and covalent solids, for example, the conflict between the cohesive energy and vacancy formation energy [14], unrealistic zero Cauchy pressures for cubic structures [14], unphysically low stacking-fault energies (SFEs) for fcc and hcp metals, and instability for diamond structures [15]. To remedy such deficiencies, two groups of improved potential models have been proposed, including the group of pair-functional potentials to introduce the long-range many-body interactions, e.g., embedded-atom method (EAM) [16], tight-binding (TB) [17,18], and Finnis-Sinclair (FS) [19] potentials, and the group of cluster potentials, which contains the short-range angular-dependent terms, e.g., Stillinger-Weber (SW) [15], Tersoff [20–22], and Brenner potentials [23].

The fundamental concept behind the former group is that the delocalized electrons in metallic solids are strongly affected by neighboring atoms as the local configuration becomes more crowded [12]; thus, interactions between the central atom and the environment (many-body contribution) need to be introduced. By treating the central atom as an impurity embedded in a host created by its neighboring atoms,

*Corresponding author: zrf@buaa.edu.cn

Daw and Baskes [16] introduced the embedding energy in the EAM model, which effectively addressed the issues related to the relaxed surface energies [16], surface composition profiles [24], and point-defect properties [25]. Similarly, yet from a different physical approximation, the TB model was proposed based on second-moment approximation [17,18,26–28], while the Finnis-Sinclair model [19] originated from the correlation between the bonding energy and the hopping integrals. Both potential models have found extensive applications in atomic-scale mechanistic simulations of metallic solids, such as plastic flow [29], dislocation nucleation [5,6,30], superior shock [31], and radiation resistance [2] with great success. The key to their effectiveness lies in incorporating long-range many-body effects, allowing for the accurate representation of the delocalized nature of electrons in metallic systems. However, it is worth noting that these potentials encounter challenges when dealing with certain transition metals with strongly overlapped *d* orbitals [32–34], which necessitates the inclusion of the angular-dependent terms of neighboring atoms [35–38].

In contrast to the first group, the short-range cluster potentials primarily focus on the directional covalent bonding and the localized nature of valence electrons by emphasizing their angular-dependent characteristics. A notable example is the classical Stillinger-Weber model [15] that characterizes the interatomic interaction in Si semiconductors by considering the angular dependence, and further simulation proves its success in qualitatively describing local liquid order. The Tersoff potential [20,21], which introduces the bond-order functional form that depends on the angular contribution, has yielded results in agreement with the experiments in the diffusion and interstitial migration of C in Si [22], and it has been extended to hcp structure metals, like Ti [39,40], Zn [37], and Zr [41]. A further refined version of the Tersoff potential is the Brenner potential, which replaces the original repulsion and attraction terms with a more physical Morse-like function and has proven better agreement of intramolecular bonding of graphite and diamond [23]. Overall, the reliability of short-range cluster potentials stems from the accurate reflection of the directional covalent bonding with localized valence electrons; however, they encounter significant challenges when modeling nonequilibrium and defective local structure [42] due to the limitation within first-neighboring atoms. As commented by Los and Fasolino [43], because C is smaller than Si, a stronger coupling between the free orbitals of undercoordinated neighboring atoms exists, and long-range correction is required [43]. On the other hand, other studies have shown that short-range cutoff results in the following problems: (1) no energy difference is observed between cubic and hexagonal diamonds, and the intrinsic stacking fault energy (ISFE) is consistently zero [44], (2) unphysical local minima appear in the generalized stacking-fault energy (GSFE) curve [42,45], and (3) inconsistency arises between unstable stacking-fault energy (USFE) and cleavage energy [45]. In addition, although the pair potential can be much improved for transition metals after introducing the angle correction, the use of a short cutoff radius disregards the intrinsic long-range interactions, which leads to the incorrect phase stability for hcp metals with high *c/a* ratios, like Zn [38,46–48].

By considering the distinct advantages of both groups of potentials, i.e., the long-range many-body effects for the former and short-range angle dependence for the latter, one may wonder the possibility of combining them to overcome the deficiency of both types of potential and enhance their capabilities based on their respective bonding characteristics. Here, by incorporating the long-range many-body effect into pair-functional potentials and the short-range angular-dependent terms into cluster potentials, a unified hybrid potential model is accordingly proposed for both metallic and covalent bonding solids, which has been demonstrated by a series of elemental solids, including 12 metals (including fcc, bcc, and hcp metals) and three covalent solids with reliable mechanical property reproduction, which suggests that the hybrid potential model possesses high compatibility for various metallic and covalent systems. Several critical issues in specific cases have also been resolved after integrating the two physical concepts, including the incorrect phase stability for metals with high *c/a* ratios and the conflict between the correct sequence order of SFEs and cleavage energy for covalent solids. In addition, the unified expression in the hybrid potential model facilitates the construction of the cross potential, which has been easily extended to compounds such as CuNi, TiC, and BN, indicating its flexibility for simulations of multielemental compound/solution systems. Furthermore, as the long-range computation in the hybrid model is limited to the pair-functional term, the total computation remains comparable to that of the two original models without the computational cost catastrophe when increasing the cutoff in the angle-dependent term. The hybrid potential model can be transformed into different formats for the simulation codes like LAMMPS [49] and SPaMD [50]. This paper is organized as follows: In Sec. II, the theoretical background of the hybrid potential model is described with the optimization scheme. In Sec. III, the critical validation and applications of the hybrid potential model are presented with several examples. Then, the results are discussed in Sec. IV. Finally, the conclusions are presented in Sec. V.

II. METHOD

A. Hybrid potential model

As each potential group originates from different physical pictures and is successful in its respective systems, one could leverage their respective advantages by selecting the classical EAM [16] and Tersoff model [20–22] to construct a hybrid potential, and the total energy is expressed as follows:

$$E_{\text{tot}} = \sum_i F_i(\bar{\rho}_i) + \frac{1}{2} \sum_i \sum_{i \neq j} \Phi_{ij(k)}, \quad (1)$$

where $F_i(\bar{\rho}_i)$ is the long-range pair-functional term for the many-body contribution in the EAM model, and $\Phi_{ij(k)}$ represents the short-range angular-dependent terms from the Tersoff model, which includes three-body interactions. As clarified by Daw and Baskes, $F_i(\bar{\rho}_i)$ is regarded as an impurity atom embedded in the host electron cloud contributed by the neighbors, which defines the embedding energy of the

impurity atom [16]. The embedding function is expressed with the universal logarithmic function [51–53] as follows:

$$F_i(\bar{\rho}_i) = F_i^e \left[1 - \eta_i \ln \left(\frac{\bar{\rho}_i}{\rho_i^e} \right) \right] \left(\frac{\bar{\rho}_i}{\rho_i^e} \right)^{\eta_i}, \qquad (2)$$

where F_i^e and η_i are fitting parameters that depend on the elements and $\rho_i^e = 1.0$ for simplicity. Moreover, $\bar{\rho}_i$ is the electron density at the site of atom i, which depends on the surrounding atoms and can be approximated by the contributions from the neighbors, i.e.,

$$\bar{\rho}_i = \sum_{i \neq j} \rho_{ij}(r_{ij}), \qquad (3)$$

where r_{ij} is the distance between atoms i and j, and ρ_{ij} is described by an exponential function as follows [3,54–56]:

$$\rho_{ij}(r_{ij}) = \rho_{ij}^d \exp\left[-\beta_{ij}^e \left(\frac{r_{ij}}{r_{ij}^e} - 1 \right) \right] S_{ij}^{(1)}(r_{ij}), \qquad (4)$$

where ρ_{ij}^d and β_{ij}^e are fitting parameters, r_{ij}^e is the is the equilibrium distance between the nearest neighbors, and $S_{ij}^{(1)}(r_{ij})$ is the trigonometric cutoff function [20,57] defined as follows:

$$S_{ij}^1(r_{ij}) = \begin{cases} 1 & , r_{ij} \leqslant r_{ij}^c - r_{ij}^s \\ \frac{1}{2} + \frac{1}{2} \cos\left(\frac{r_{ij} - r_{ij}^c + r_{ij}^s}{r_{ij}^s} \pi \right) & , r_{ij}^c - r_{ij}^s \leqslant r_{ij} \leqslant r_{ij}^c \\ 0 & , r_{ij} > r_{ij}^c \end{cases} \qquad (5)$$

This function is continuous for all ranges of r_{ij} and ranges from one to zero within the cutoff, and here $r_{ij}^s = 0.02 r_{ij}^c$ for simplicity.

Following the Tersoff model for the three-body interactions, the short-range angular-dependent term is expressed as

$$\Phi_{ij(k)} = f_{ij}^R(r_{ij}) + b_{ij(k)} f_{ij}^A(r_{ij}), \qquad (6)$$

where the repulsive interaction $f_{ij}^R(r_{ij})$ includes the orthogonalization energy when electron clouds overlap [20] and is expressed as

$$f_{ij}^R(r_{ij}) = \frac{D_{ij}^{(0)}}{S_{ij} - 1} \exp\left[-\mu_{ij} \sqrt{2 S_{ij}} \left(r_{ij} - r_{ij}^{(0)} \right) \right] S_{ij}^{(2)}(r_{ij}). \qquad (7)$$

Moreover, $f_{ij}^A(r_{ij})$ represents an attractive interaction associated with bonding and is expressed as follows:

$$f_{ij}^A(r_{ij}) = -\frac{S_{ij} D_{ij}^{(0)}}{S_{ij} - 1} \exp\left[-\mu_{ij} \sqrt{2/S_{ij}} \left(r_{ij} - r_{ij}^{(0)} \right) \right] S_{ij}^{(2)}(r_{ij}), \qquad (8)$$

where $D_{ij}^{(0)}$, $r_{ij}^{(0)}$, μ_{ij}, and S_{ij} are fitting parameters, and the pair term reduces to the usual Morse potential when $S_{ij} = 2$ [23].

The smooth cutoff function $S_{ij}^{(2)}(r_{ij})$ is expressed as

$$S_{ij}^{(2)}(r_{ij})$$
$$= \begin{cases} 1 & , r_{ij} \leqslant R_{ij} - D_{ij} \\ \frac{1}{2} - \frac{1}{2} \sin\left(\frac{r_{ij} - R_{ij}}{D_{ij}} \frac{\pi}{2} \right) & , R_{ij} - D_{ij} \leqslant r_{ij} \leqslant R_{ij} + D_{ij}. \\ 0 & , r_{ij} > R_{ij} + D_{ij} \end{cases}$$
$$(9)$$

The prefactor $b_{ij(k)}$ in Eq. (6) is usually interpreted as the bond-order term, which reflects the covalent bonding character and is assumed to be a monotonically decreasing function of the coordination of atoms i and j [20–22]:

$$b_{ij(k)} = \left[1 + \left(\beta_{ij} \sum_{k \neq i,j} \xi_{ijk} \right)^{n_{ij}} \right]^{-1/2n_{ij}}, \qquad (10)$$

where

$$\xi_{ijk}(r_{ij}, r_{ik}, \theta_{ijk}) = S_{ij}^{(2)}(r_{ij}) g_{ijk}(\theta_{ijk}) \exp\left[\lambda_{3,\,ijk}^m (r_{ij} - r_{ik})^m \right], \qquad (11)$$

$$g_{ijk}(\theta_{ijk}) = \gamma_{ijk} \left(1 + \frac{c_{ijk}^2}{d_{ijk}^2} + \frac{c_{ijk}^2}{d_{ijk}^2 + \left(\cos\theta_{ijk} - \cos\theta_{ijk}^{(0)} \right)^2} \right), \qquad (12)$$

and θ_{ijk} represent bond angle between bonds ij and ik; β_{ij}, n_{ij}, γ_{ijk}, $\lambda_{3,\,ijk}$, c_{ijk}, d_{ijk}, and $\cos\theta_{ijk}^{(0)}$ are fitting parameters. Table I compares the potential parameters of the representative elements of Cu (fcc), Fe (bcc), Ti (hcp), and C (diamond) for the hybrid model and those from the Tersoff [58] or baseline EAM for comparison. Notice that the baseline EAM potential could be readily obtained by transforming the three-body term $\Phi_{ij(k)}$ to a pair function $\Phi_{ij}(r_{ij})$ through setting the β_{ij} parameter to zero. With the baseline EAM as a reference, it can be seen clearly that after removing the angular-dependence term, the three-body interaction is partially incorporated into the many-body term, as evidenced by the increasing F^e parameter associated with the embedding energy and the decreasing $D^{(0)}$ parameter associated with the three-body interaction. Here, F_i^e plays a critical role in controlling the relative contributions of short-range angular dependence and long-range n-body effect to the total energy, as shown in Table II. These results indicate that the short-range angular-dependence term contributes more to the total potential energy for the covalent systems, which results in smaller values of $\frac{|F_i(\bar{\rho}_i)|}{E_c}$ ranging from 0.24 to 0.27 for Si, C, and TiC, whereas the contribution of embedding energy term takes up a larger portion of total energy, which varies from 0.36 to 0.54 for Ti, Cu, Ni, and their alloy. Moreover, it can be observed that group 10 metals with unpaired d electrons exhibit stronger many-body effects compared to the group 11 ones with full d subshell, and the influence of the many-body effect becomes more pronounced as the period number increases, corresponding to the expansion of the d-shell electrons. For instance, the values of $\frac{|F_i(\bar{\rho}_i)|}{E_c}$ for Cu, Ag, and Au are 0.30, 0.31, and 0.40, respectively; the only exception is Pd, which may be attributed to its unique electronic configuration, i.e., a completely filled

TABLE I. Potential parameters of representative elements of Cu (fcc), Fe (bcc), Ti (hcp), and C (diamond) from hybrid model and those from baseline EAM or Tersoff [3,58] models for comparison (see Supplemental Material for complete parameter tables [67]; see also Refs. [3,39,40,42,45,55,59,75,77–97] therein).

		Cu		Fe		Ti		C	
		Hybrid	Baseline EAM	Hybrid	Baseline EAM	Hybrid	Baseline EAM	Hybrid	Tersoff
m		1.0		1.0		1.0		3	3
γ		1.0	0.0	1.0	0.0	1.0	0.0	1.0	1
λ_3	Å^{-1}	1.62883		0.631352		0.135518		0.731207	0
c		0.735724		1.15779		1.05450		41969.3	38049
d		0.128546		0.226254		0.281135		5.19033	4.3484
$\cos\theta^{(0)}$		−1.0		−0.635993		−0.867527		0.538488	0.57058
n		1.0		1.0		1.0		0.72751	0.72751
β		0.000902788	0.0	0.00189476	0.0	0.00204566	0.0	1.22528×10^{-7}	1.57×10^{-7}
μ	Å^{-1}	1.61149	2.20972	1.17846	1.43991	1.18117	1.99612	1.15776	1.964037
S		1.38141	1.84776	1.42630	1.30261	1.22663	1.39634	1.39070	1.576879
R	Å	4.02123	4.02123	3.42818	3.42818	3.50796	3.507956	2.12084	1.95
D	Å	0.203113	0.203113	0.294092	0.294092	0.292081	0.292081	0.394575	0.15
$r^{(0)}$	Å	2.39264	2.63864	2.37977	2.64556	2.64493	2.91182	1.67404	1.447114
$D^{(0)}$	eV	0.63917	0.131632	0.850178	0.529209	1.00787	0.323114	3.94443	5.166175
ρ^d		0.0672419	0.03662	0.0508864	0.0179783	0.0309789	0.0903512	0.0894240	
β^e		4.30500	3.65975	3.81579	6.37375	3.16782	3.81369	2.38696	
F^e		1.07161	2.75121	2.35005	2.91173	2.36157	3.61219	2.39077	
η		0.651824	0.506107	1.34550	0.509394	0.850190	0.775665	3.02842	
r^e	Å^{-1}	2.55619	2.55619	2.45951	2.45951	2.92379	2.92379	1.54746	
r^s		5.99480	5.99480	5.93482	5.93482	6.85690	6.85690	6.00855	

$4d^{10}$ shell instead of the $5s^2\,4d^8$ configuration. To quantify the term $b_{ij(k)}$, Fig. 1(a) shows the variation of $\beta_{ij} \cdot \xi_{ijk}$, which exhibits a higher angular correlation for C than that for Ti, in consistency with a strong covalent bonding nature for the former one; Fig. 1(b) illustrates that Ni ($4s^2\,3d^8$) exhibits a higher angular effect than Cu ($4s^1\,3d^{10}$), which stems from the complexity of the mixed metallic and covalent bonding owing to the overlapping d orbitals [33], where valence d electrons remain relatively tightly bound to their parent atoms, forming unsaturated covalent bonds with their neighbors [32]. Notably, although the group 10 metals exhibit a higher angular effect relative to the group 11 metals, less covalent direction-

ality association exists when compared to Al, which is limited with respect to the typically directional bonding elements.

In terms of the cross-potential construction, the elemental hybrid potentials may be seamlessly combined by using the scale-invariance rule, which involves an additional step to fit the cross term Φ_{ab} through the properties of simple compounds with low formation energy, preferably observed in experiments. To retain the reliability of the original elemental potentials, the adopted scale-invariance rule is as follows:

$$\rho'_{aa}(r_{ij}) = s_{aa}\rho_{aa}(r_{ij}), \tag{13}$$

$$F_{aa}'(\bar{\rho}'_i) = F_{aa}(\bar{\rho}'_i / s_{aa}), \tag{14}$$

where s_{aa} is the fitting parameter, and it is only used in the construction of cross potential but not required for elemental

TABLE II. Comparison of parameters of F_i^e, embedding energies $|F_i(\bar{\rho}_i)|$, cohesion energies E_c, and their ratios of representative covalent and metallic systems.

System	Si	C	TiC	Ti	Cu$_3$Ni	CuNi$_3$	
structure	diamond	diamond	B$_1$	hcp	L1$_2$	L1$_2$	
F_i^e	1.49	2.39		2.36			
$|F_i(\bar{\rho}_i)|$	1.07	2.07	2.06	2.13	1.46	2.23	
E_c	4.40	7.85	7.40	5.38	3.86	4.51	
$\frac{|F_i(\bar{\rho}_i)|}{E_c}$	0.24	0.26	0.27	0.40	0.38	0.50	
System	Cu	Ni	Ag	Pd	Au	Pt	Al
structure	fcc	fcc	fcc	fcc	fcc	fcc	fcc
F_i^e	1.07	2.63	0.79	1.41	1.20	3.54	1.45
$|F_i(\bar{\rho}_i)|$	1.07	2.62	0.78	1.37	1.18	3.54	1.41
E_c	3.55	4.86	2.49	3.73	2.98	5.52	3.50
$\frac{|F_i(\bar{\rho}_i)|}{E_c}$	0.30	0.54	0.31	0.37	0.40	0.64	0.40
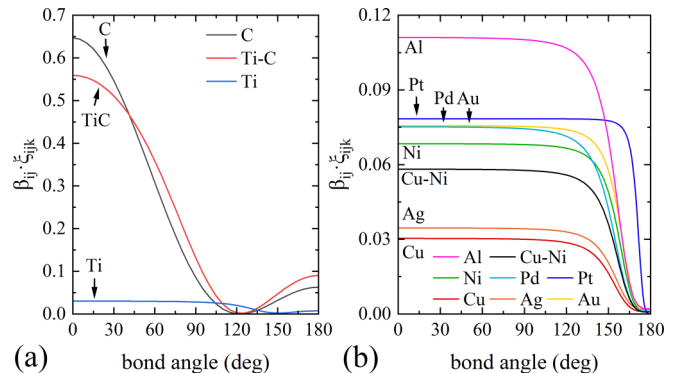
FIG. 1. Correlation between parameter $\beta_{ij} \cdot \xi_{ijk}$ and bond angles of (a) TiC and (b) various metal elements.
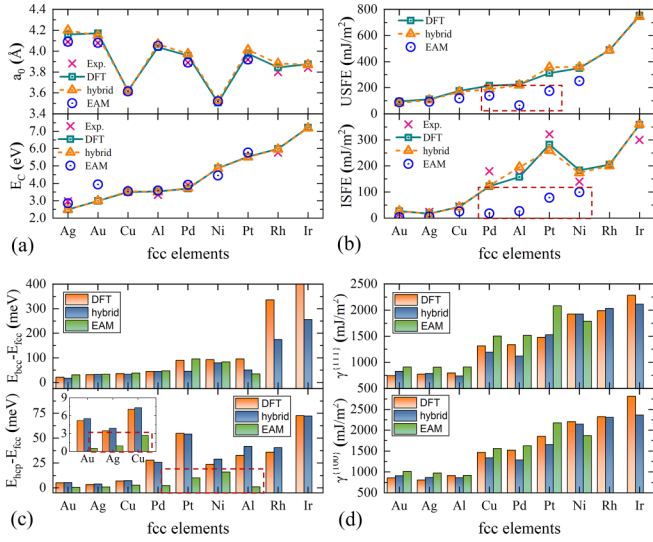
FIG. 2. (a) Lattice constants, cohesive energies, (b) intrinsic stacking fault energy (ISFE), unstable stacking fault energy (USFE), (c) relative phase energies, and (d) surface formation energies for fcc metals with hybrid potential alongside DFT data, experimental data, and those of Zhou *et al.* [3] for comparison; EAM, embedded-atom method.

FIG. 3. (a) Lattice constants, cohesive energies, (b) USFE of {110} and {112} planes, (c) relative phase energies, and (d) surface formation energies for bcc metals with hybrid potential alongside DFT data, experimental data, and those of Zhou *et al.* [3] for comparison.

potentials. The scale-invariance rule increases the flexibility to combine two elemental hybrid potentials. In addition, since the parameters of s_{aa} and s_{bb} for the two-component elements are closely correlated, it is sufficient to scale the charge density ρ for one-component element, and the scale parameter for the one-component element was always chosen to be 1.0 [59,60].

B. Potential optimization

Figure S1 illustrates the core stages involved in constructing the hybrid potential of preparation, initialization, and optimization. At the preparation step, all training targets are prepared according to the experimental or DFT data. According to the fitting strategy, not all potential parameters need to be involved in the optimization process because optimizing some critical parameters first and the remaining parameters thereupon may lead to more reliable results [42]; thus, a custom parameter map [45] was introduced to control the degree of free parameters for custom optimization strategy at the initialization step. At each optimization step, adjustable fitting parameters are varied first and then (1) executed custom mapping to update potential parameters and (2) tabulated potential and computed all related properties to evaluate the predefined cost function. Finally, the constructed potential is validated by further property checks and then saved in a tabulated potential form adapted to simulation software.

The optimization quality depends on the minimization process by a cost function that quantifies the difference between the prediction and training sets, which is defined by the least-squares method in this work:

$$Z_{tot} = \sum_{k=0}^{N} w_k \left(\frac{A_k^{predict} - A_k^{target}}{A_k^{target}} \right)^2, \quad (15)$$
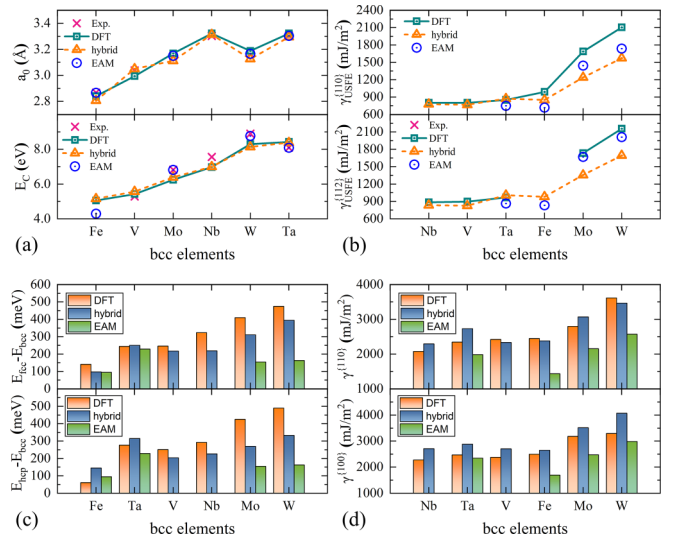
where $A_k^{predict}$ is the kth prediction property, A_k^{target} is the kth target value, and w_k is the corresponding weight factor to control the optimization quality, as shown in Table SI. In general, with different requirements of realistic simulations adapted to certain simulation environments, one may pay more attention to the most relevant quantities in fitting the undetermined parameters for hybrid potentials. For instance, in terms of mechanical simulations, the fitting targets include at least the lattice constants, cohesive energy, lattice stabilities, elastic constants, surface energies, and SFEs. In the case of covalent materials, a higher weighting factor used for SFEs and cleavage energy is based on the following facts: (1) the SFEs of covalent materials are orders of magnitude higher than that of metallic materials, as well as the cleavage energy of the former is also much higher than that of the latter; and (2) the cleavage energy is essential in cracking simulations of brittle materials, whereas the dislocation mobility dominates in metals.

The optimization process was conducted by using the EAPOT platform [45,61] with the Nelder-Mead simplex method [62]. For more details on the potential optimization step, one can refer to the previous publications [45,61]. It should be noted that the adjustment in the weight-factor configuration [63,64] will have a certain impact on the predicted value, whose selection is related to history with certain experiences [59,65,66], and the current hybrid model is still challenging to unify different systems.

III. RESULTS

A. Validation of hybrid potentials for single-element solids

As a first demonstration, the hybrid potential model should be able to reproduce the fundamental properties of single-element solids. Figures 2–4 present the predicted structural and physical properties of representative fcc, bcc,
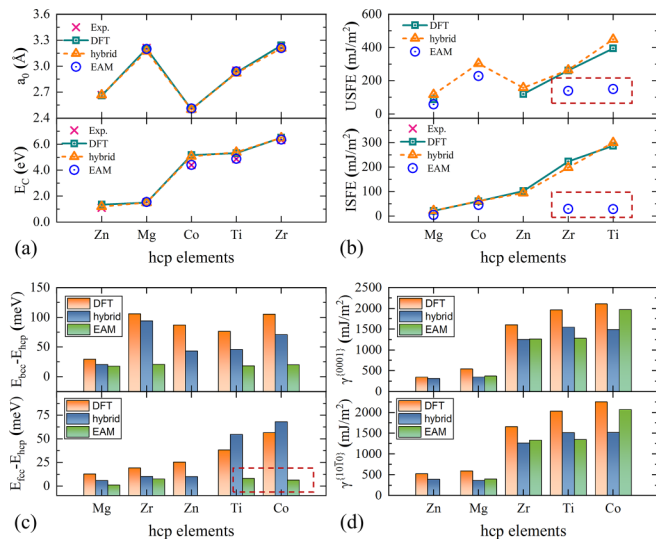
FIG. 4. (a) Lattice constants, cohesive energies, (b) ISFE, USFE, (c) relative phase energies, and (d) surface formation energies for hcp metals with hybrid potential alongside DFT data, experimental data, and those of Zhou *et al.* [3] for comparison.

and hcp metals from the optimized hybrid potentials and those proposed by Zhou *et al.* [3] for comparison between the experimental and theoretical data. All detailed values in the above figures and fitted potential parameters are listed in Tables SII–SVII for reference [67]. Compared to previous studies [3,59,66,68], the hybrid potentials provided an improved description of fcc, bcc, and hcp metals, particularly regarding the lattice stability between compact stacking structures and SFEs. For instance, the predicted energy differences between fcc and hcp phases ($E_{hcp} - E_{fcc}$) for Au, Pd, and Pt by hybrid potential are 5.6, 25.6, and 54.0 meV, respectively, which closely match the DFT values of 5.5, 27.9, and 54.9 meV, respectively. By contrast, the corresponding values from Zhou's EAM potentials [3] are 0.5, 2.5, and 10.1 meV, respectively, and exhibit deviations of 90, 90, and 82%, respectively, from the DFT values [see the dashed box in Fig. 2(c)]. As shown in Fig. 3, the predicted energy differences $E_{fcc} - E_{bcc}$ for the bcc Mo and W by the hybrid potentials are 311 and 394 meV, respectively, with the DFT data being 409 and 474 meV, respectively, yet twice larger than those obtained from Zhou's EAM potentials (154 and 163 meV, respectively). More impressively, the ISFE values of hcp Mg, Zr, and Ti by the hybrid potential are approximately 22, 198, and 300 mJ/m², respectively, and agree well with the DFT values (21, 233, and 287 mJ/m², respectively), in contrast to those predicted by Zhou's EAM (4, 29, and 28 mJ/m², respectively) [3] [see the dashed box in Fig. 4(b)]. In addition, the hybrid potentials provide desirable USFE values (see Fig. 5), which presents the GSFE curves along the [112] direction alongside the DFT and EAM data for comparison; obviously, the GSFE curves of the hybrid potentials agree well with the DFT in both shape and quantity. All the consistency suggests that the constructed hybrid potentials could provide a more desirable description of fundamental quantities that are related to the mechanical simulations, particularly for dislocation structure and behavior.

The capability of the present hybrid potential model can also be ascertained by solving the difficulties that are met when purely using pair-functional potentials or cluster potentials. Table III summarizes the reproduced properties of Zn with the hybrid potential and compares them with the EAM potential by Sheng *et al.* (S.EAM) [69,70], FS potential by Igarashi *et al.* (I.FS) [71], modified embedded-atom method (MEAM) potential by Dickel *et al.* (D.MEAM) [48], MEAM potential by Jang *et al.* (J.MEAM) [38], Tersoff potential by Erhart *et al.* (E.Tersoff) [37], and bond-order potential (BOP) by Ward *et al.* (W.BOP) [72]. Obviously, both the long-range pair-functional potential and the short-range cluster potential face critical difficulties in achieving reasonable lattice stability for hcp Zn owing to its high *c/a* ratio. Among the six potentials, only S.EAM, I.FS, and D.MEAM predicted a *c/a* ratio comparable to experimental and DFT data, whereas J.MEAM, E.Tersoff, and W.BOP predicted only the ideal one (*c/a* = 1.63), which may result in ultralow resistance for basal twinning modes during deformations [38]. However, S.EAM, I.FS, and D.MEAM cannot guarantee the stability of hcp Zn, and the predicted ISFEs of −4.2, 0.4, and −98 mJ/m² are far lower than the DFT value of 102 mJ/m², indicating that they are unsuitable for plastic simulations. In fact, Baskes and Johnson [46,47] have long noted the failure of MEAM formalism in reproducing the correct ground state when the *c/a* ratio for the hcp structure is greater than the ideal [48]. A similar issue occurs in the Tersoff model, e.g., the E.Tersoff potential [37] predicted the stable hcp structure with *c/a* = 1.63, which is far from the DFT value of 1.903. Although the long-range pair-functional potentials consider more distant atoms, their spherically symmetric assumption fails to provide a reasonable *c/a* ratio for hcp Zn, e.g., the S.EAM potential does not guarantee the stability of hcp Zn. According to first-principles calculations, the anomalous *c/a* ratio in Zn is attributed to the electronic correlation, where the filled *d* shell not only screens the nuclear charge but is explicitly involved in the correlation interactions [73], and the later works showed that the experimentally known anisotropic minimum could only be obtained after using the three-body increment method for *d*-correlation contributions [74]. However, the pair-functional potentials or cluster potentials only partially capture the long-range many-body or angular effect of the complex *d* shell, thus failing to describe phase stability for Zn with a high *c/a* ratio, consistent with the observation by Baskes *et al.* that "the nature of the MEAM formalism, makes it impossible to create a potential with simultaneously lower hcp cohesive energy than fcc and a *c/a* ratio greater than the ideal" (see Fig. S2) [46,48]. To address these limitations, the hybrid potential model incorporates the long-range many-body effect in pair-functional potentials and the short-range angular-dependent terms in cluster potentials, thereby achieving reasonable lattice stability for elemental metals with high *c/a* ratios. As shown in Table III, although the relative phase energy is lower than the DFT value of 25.4 meV, the hybrid potential ensures the stability of the hcp phase and reasonable SFE values, accompanied by a *c/a* ratio of 1.905, which closely matches the DFT and experimental data of 1.903.

The efficiency of the hybrid potential model is then evaluated for representative covalent elemental solids. Table IV presents the physical properties of the C, Si, and Ge systems
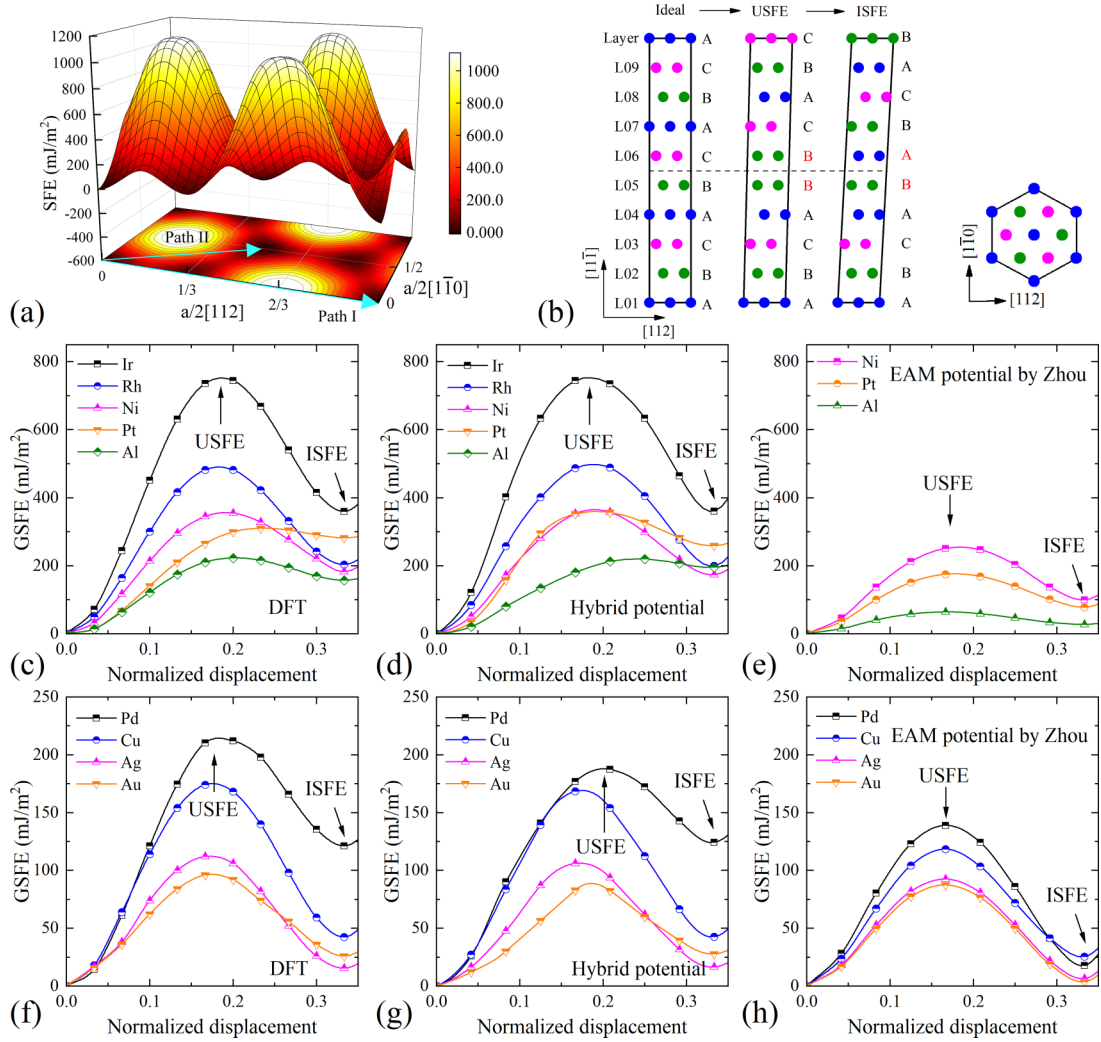
FIG. 5. (a) Typical γ surface of the {111} plane for Cu. (b) Schematic illustration of stacking sequences of perfect lattice, USFE, and ISFE (c), (d) Generalized stacking fault energy (GSFE) curves along [112] directions with marked USFE and ISFE values by DFT calculations [80,81], hybrid potentials, and EAM potentials of Zhou *et al.* [3] for comparison; SFE, stacking fault energy.

TABLE III. Lattice constants, *c/a* ratio, cohesive energies, vacancy formation energies, elastic constants, ISFE, USFE, surface formation energies, and relative phase energies for Zn with hybrid potential alongside DFT data, experimental data, and previous studies for comparison.

	a_0 (Å)	c/a	E_C (eV)	E_V (eV)	C_{11} (GPa)	C_{12} (GPa)	C_{13} (GPa)	C_{33} (GPa)	C_{44} (GPa)	γ_{USFE} (mJ/m²)	γ_{ISFE} (mJ/m²)	$\gamma^{\{0001\}}$ (mJ/m²)	$E_{fcc} - E_{hcp}$ (meV)	$E_{bcc} - E_{hcp}$ (meV)
Exp.	2.660[a]	1.86[a]	1.35[a]	0.54[b]	179[c]	38[c]	55[c]	69[c]	46[c]					
DFT	2.647[a]	1.905[a]	1.10[a]	0.48[b]	160[d]	56[d]	52[d]	57[d]	23[d]	120[e]	102[e]	347[f]	25[g]	87[g]
Hybrid	2.668	1.903	1.19	0.20	131	72	31	74	26	157	94	311	10.0	43
EAM [69,70]	2.602	1.932	1.35	1.81	145	67	61	102	12	24	−4.2	302	−1.6	89
FS [71]	2.778	1.860	1.35	0.42	179	38	55	69	46		0.4			
MEAM [48]	2.647	1.872	1.35	1.55	123	36	63	86	51	162	−98	591	−35	49
MEAM [38]	2.778	1.619	1.09	0.44	120	48	42	133	34	163	45	446	9.2	79
Tersoff [37]	2.700	1.629	1.33	0.26	426	215	185	465	97	133	26	347	5.0	125
BOP [72]	2.761	1.717	1.56	0.61	192	22	20	136	37				246	15

[a]Reference [86].
[b]Reference [82].
[c]Reference [83].
[d]Reference [112].
[e]Reference [87].
[f]Reference [84].
[g]Reference [85].

TABLE IV. Lattice constants (Å), cohesive energies (eV), elastic constants (GPa), ISFE (J/m²), USFEs (J/m²), cleavage energies (J/m²), surface formation energies (J/m²), and relative phase energies of $E_{hdia} - E_{cdia}$ (meV) for covalent solids with hybrid potential alongside DFT data and other studies for comparison [42,75,76].

		C			Si			Ge		
		DFT	Hybrid	Tersoff [75]	DFT	Hybrid	Tersoff [75]	DFT	Hybrid	Tersoff [76]
Cubic	a_0	3.574[a]	3.589	3.556	5.469[a]	5.513	5.432	5.763[a]	5.833	5.553
diamond	E_C	7.83[a]	7.85	7.47	4.60[a]	4.40	4.63	3.74[a]	3.60	4.23
	C_{11}	1054[a]	1007	1008	144[a]	137	143	104[a]	111	214
	C_{12}	126[a]	130	169	53[a]	62	75	37[a]	38	21
	$C440$	564[a]	382	545	99[a]	93	119	72[a]	68	106
	C_{44}	562[a]	381	462	75[a]	68	69	56[a]	54	92
	$\gamma_{USFE}^{\{111\}[112]}$	5.78[b]	7.58	13.36	1.82[b]	2.00	2.01	1.55[b]	1.47	3.01
	$\gamma_{ISFE}^{\{111\}[112]}$	0.28[b]	0.02	0.00	0.04[b]	0.01	0.00	0.07[b]	0.01	0.00
	$\gamma_{USFE}^{\{111\}[110]}$	9.97[b]	10.12	10.96	1.45[b]	1.73	2.40	1.10[b]	1.23	2.53
	$\gamma_{USFE}^{\{110\}[110]}$	13.76[c]	14.21	13.46	1.70[b]	1.93	3.14	1.34[b]	1.40	3.11
	$\gamma_{USFE}^{\{100\}[110]}$	16.81[c]	17.60	17.22	2.32[b]	2.28	4.54	1.66[b]	1.79	4.39
	$E_b^{\{111\}}$	14.40[c]	14.54	10.93	3.30[d]	3.95	2.57	2.17[d]	2.88	2.54
	$\gamma^{\{111\}}$	5.65[c]	6.74	5.46	1.57[d]	1.95	1.20	1.11[d]	1.42	1.27
Hexagonal	a_0	2.51[a]	2.54	2.51	3.85[a]	3.90	3.84	4.05[a]	4.13	3.93
diamond	c_0	4.18[a]	4.14	4.11	6.37[a]	6.36	6.27	6.68[a]	6.75	6.41
	$E_{hdia} - E_{cdia}$	25[a]	1.2	0.0	11[a]	0.9	0.0	119[a]	0.9	0.0
	C_{11}	1189[a]	943	1064	182[a]	141	175	127[a]	104	212
	C_{12}	97[a]	144	141	49[a]	41	66	32[a]	22	19
	C_{13}	13[a]	167	140	34[a]	27	52	17[a]	17	24
	C_{33}	1295[a]	927	1065	203[a]	123	190	147[a]	96	207
	C_{44}	458[a]	422	434	49[a]	38	45	37[a]	35	95

[a]Reference [78].
[b]Reference [113].
[c]DFT calculations in this work.

predicted by the hybrid potentials and the previous Tersoff potentials [42,75,76], which are compared with the DFT values. Apparently, the hybrid potentials could reasonably reproduce the DFT calculations (the potential parameters are listed in Table SVIII in Supplemental Material [67]; see also Refs, [3,39,40,42,45,55,59,75,77–97], therein). Although the predicted ISFE of 0.02 J/m² by the developed hybrid potential underestimates the DFT values of 0.28 J/m² for C, it resolves the zero-value problem encountered with the previous Tersoff potential owing to its short-range truncation [44]. In addition, although the Tersoff C potential [75] predicted reasonable cleavage energy of 10.93 J/m² (close to the DFT value of 14.40 J/m², as shown in Table IV), the predicted USFE along the {111} [112] slip system (13.36 J/m²) is higher than that along the {111} [110] slip system (10.96 J/m²), in contrast to the corresponding DFT values (5.78 and 9.97 J/m²). To demonstrate the coupling between the cleavage energy and SFE, we have tried to modify the cleavage energy individually with the other intrinsic properties fixed, and the results are shown in Fig. 6(a). It can be clearly seen that $\gamma_{USFE}^{\{111\}[112]}$ increases simultaneously as the cleavage energy increases by means of the Tersoff model, even though different optimization strategies are used. To underline the origin, the surface structure [Fig. 6(b)] and atomic configurations alongside the

GSFE curves [Figs. 6(c) and 6(d)] are compared. It is found that the coordination environment of the near-surface atoms and that of the atoms near the slip plane at the USFE site are the same under the nearest-neighbor truncation [as compared in Fig. 6(e)], indicating a strong correlation between cleavage energy and USFE. After introducing the long-range interaction, the hybrid potential model achieves reasonable cleavage energies, i.e., the cleavage energies for the cubic diamond of 14.54 J/m² agree well with the DFT values of 14.40 J/m²; moreover, the sequence of SFE is correct, i.e., $\gamma_{USFE}^{\{111\}[112]} < \gamma_{USFE}^{\{111\}[110]} < \gamma_{USFE}^{\{110\}[110]} < \gamma_{USFE}^{\{100\}[110]}$ for cubic diamond and $\gamma_{USFE}^{\{111\}[110]} < \gamma_{USFE}^{\{110\}[110]} < \gamma_{USFE}^{\{111\}[112]} < \gamma_{USFE}^{\{100\}[110]}$ for Si and Ge (see Fig. 7). All these are consistent with the DFT results.

B. Validation of hybrid potentials for compound solids

Hybrid potentials for compound solids were constructed based on the scale-invariance rule by combining elemental potentials without reliability loss, and three representative cases of CuNi, TiC, and BN cross potentials were chosen for demonstration (the potential parameters are listed in Table SIX). For the CuNi case, the equilibrium structures and properties of hypothetical simple compounds were obtained by
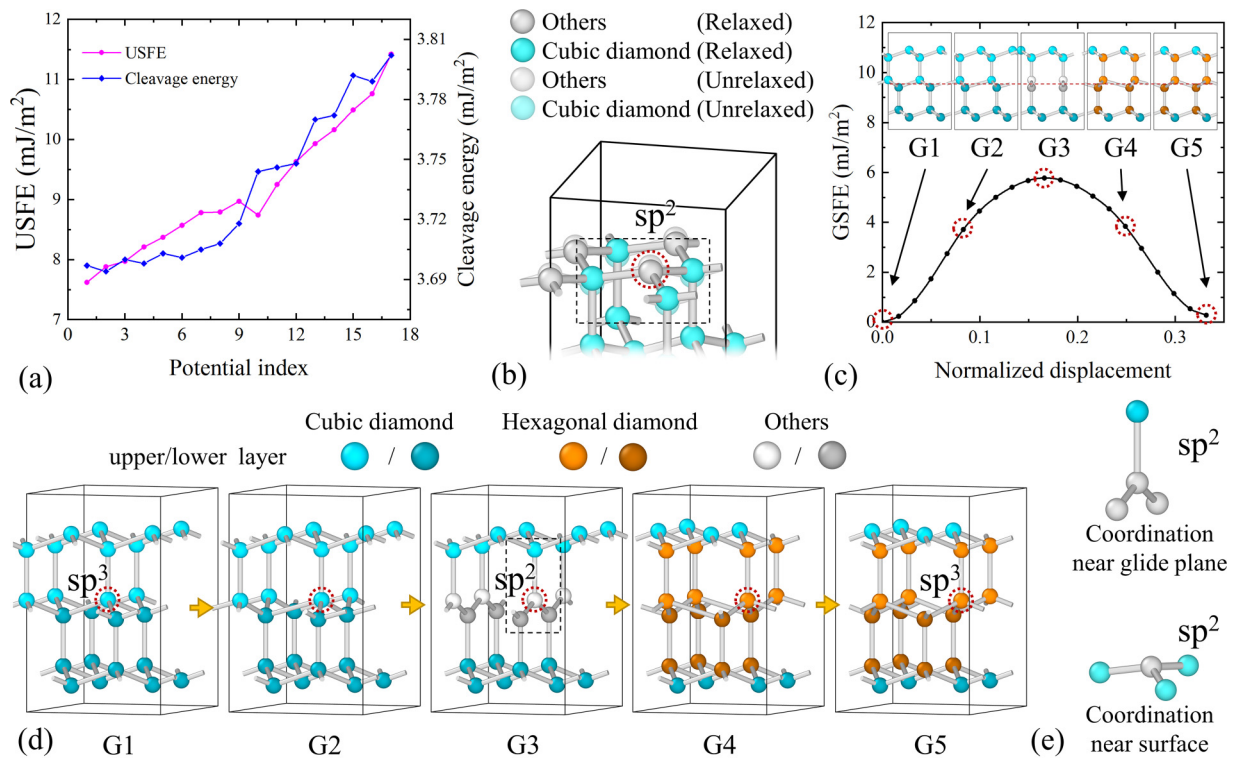
FIG. 6. (a) USFE of {111} [112] slip system and cleavage energy for constructed Tersoff potential series. (b) Surface structure of {111} glide plane by DFT calculation, where cyan and gray represent cubic diamond and other structures, respectively. Semitransparent atoms represent atomic positions before relaxation, where surface atoms tend to relax inward (i.e., toward bulk). (c), (d) GSFE curves along [112] direction on {111} planes and atomic configuration snapshots at key sites. (e) Coordination environment of near-surface atoms and that of atoms near glide plane at USFE site.

DFT calculations to compensate for the lack of experimental data. Table SX presents the predicted properties of the hybrid CuNi potential, which are compared with the DFT data, and it can be noticed that the hybrid CuNi potential could reproduce the DFT values well. For example, the hybrid potential predicted the formation energy of Cu_3Ni ($L1_2$) and CuNi (B_2) to be 18 and 83 meV, respectively, which are comparable to the DFT values of 13 and 83 meV and show better agreement than the values of -0.96 and 37 meV of the previous CuNi potential [88]. In addition to the formation energy, the elastic constants calculated by the hybrid potential agree with the DFT data with deviations of 6.7% for C_{11}, 14% for C_{12}, and 5.3% for C_{44} of $L1_2$ (Cu_3Ni) structure, in contrast to the deviations of 9.7, 19, and 19% of the other CuNi potential [88].

Considering TiC as an example of metallic and covalent systems, the cross potential was constructed based on cubic TiC, cubic Ti_2C, trigonal Ti_2C, and reduced Ti_3C_2 [77] (see Fig. S3 and, for more details, Ref. [67]). Table SXI presents the calculated properties by the hybrid potential, MEAM potential by Yao *et al.* [45], and Tersoff potential by Huang *et al.* [42], which are compared with DFT values [78,90]. It can be noted that the formation energies of cubic B_1−TiC, cubic Ti_2C, trigonal Ti_2C, and Ti_3C_2 were calculated to be -790, -663, -680, and -715 meV, respectively, by the hybrid potential, which showed reasonable agreement with the DFT values of -835, -654, -645, and -702 meV, respectively. By contrast, the calculated values of a previous MEAM potential [89] are -395, -420, and -243 meV, respectively, whereas

the values of a previous Tersoff potential are -1285, -1289, and -1065 meV, respectively [39,40], both of which significantly deviate from DFT values.

The last demonstration was performed on the construction of effective hybrid potentials of covalent compound solids to solve related issues [42,45], such as unphysical local minima in GSFE, incorrect sequence order of SFEs for the typical slip systems, and low cleavage energy. Considering the BN system as an instance, Table V and Fig. 8 present the predicted GSFE of cubic BN by the hybrid potential [67], Tersoff potential by Kınacı *et al.* [98], Tersoff potential by Huang *et al.* [42], and Tersoff potential in our previous work [45], which are compared with the DFT data. It can be observed that all the previous potentials except for that by Huang exhibit incorrect sequences of SFEs, whereas the hybrid potential [Fig. 8(b)] agrees well with the DFT data [Fig. 8(a)]. Moreover, the cracking events are observed in uniaxial compression simulations of Huang's potential without the appearance of dislocation nucleation [Figs. S4(a) and S4(b)], which can be ascribed to the underestimated cleavage energy of $7.42 J/m^2$. Although the previous BN potential [45] predicted a cleavage energy ($9.26 mJ/m^2$) more comparable to the DFT data ($13.9 J/m^2$), the USFE value along the {111} [112] slip system for partial dislocation is much higher than that along the {111} [110] slip system for full dislocation, resulting in full dislocations exclusively [see Figs. S4(c) and S4(d)]. By contrast, the constructed hybrid BN potential successfully addresses the problem [see Fig. S4(e)], i.e., the dislocation
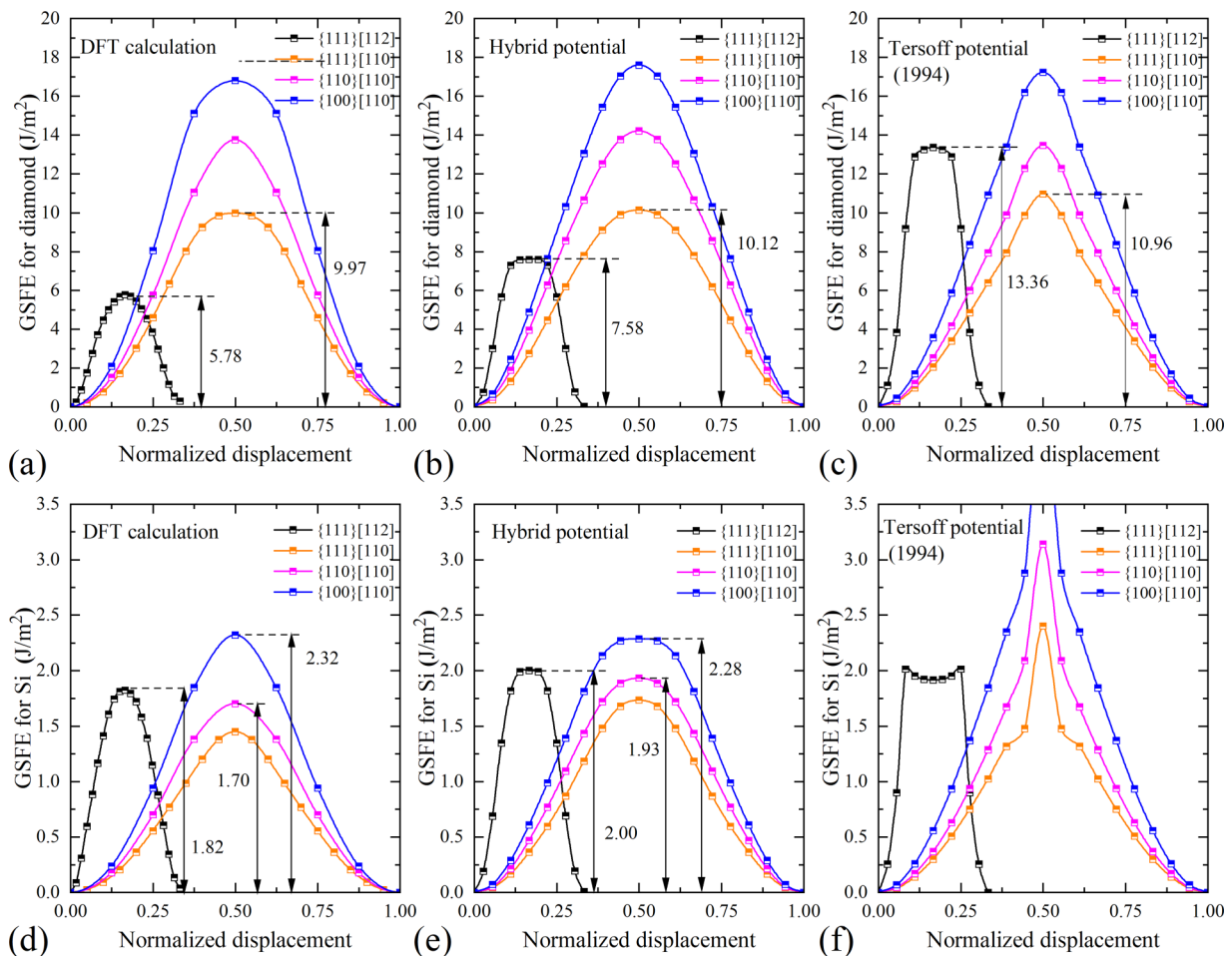
FIG. 7. GSFE curves along [112] direction on {111} planes and along [110] direction on {001}, {110}, and {111} planes of diamond with (a) DFT calculation, (b) hybrid potential, and (c) published Tersoff potential [75] and those of Si with (d) DFT calculation, (e) hybrid potential, and (f) published Tersoff potential [75].

appears before the cracking events, which is inconsistent with the DFT results [99] and experimental studies [100]. Although the full dislocations have higher barriers, they are found to dominate the plastic deformation process, which is supported by the observation that the density of full dislocations ($0.038 \, \text{nm}^{-2}$) is much higher than that of partial dislocations ($0.01 \, \text{nm}^{-2}$), being quite consistent with the experimental observation that full dislocations contribute to the plastic deformation [100]. In brief, the hybrid BN potential could provide an alternative solution to the critical issues of the previous BN potential, further validating its fidelity for covalent compound solids.

IV. DISCUSSION

The success of the hybrid potential model, as proposed in Sec. II, can be attributed to the combination of the long-range many-body effect of the metallic bonding feature and the short-range angular effect of the covalent bonding nature. Figure S5 illustrates both effects in the proposed hybrid potential model, i.e., the long-range many-body effect in pair-functional potentials and the short-range angular-dependent terms in cluster potentials. The first term in the hybrid potential model originates from the physical picture shown in

the EAM [101] that was derived from DFT [102], as well as the conclusion that the energy of an impurity in a host is a function of the electron density of a host without impurities (i.e., unperturbed host) [103]. In metals, the effective interatomic forces mediated by the conduction electron sea may extend over significant distances [104], even up to 20 atomic spacings as supported by the experimental dispersion relation [105]. Thus, a long-range functional term was generally utilized to capture the metallic-bond character; compared to previous models [37,38,69–72], the hybrid potential model has improved the prediction of phase stability for metals with high c/a ratios. As regards the short-range angular-dependent term, it is motivated by the valence-shell electron-pair repulsion (VSEPR) theory [106] and the TB theory [26]. According to the VSEPR theory, the repulsions between pairs of valence electrons due to overlapping tend to maximize bond angles, and the TB theory shows that the density of states can be efficiently determined by describing moments within Green's function framework [107–109], which can be further evaluated explicitly in terms of hopping integrals and bond angles [110]. By including the angular dependence, the Tersoff and other BOP potential models [20–22] have been successfully used for covalent solids after introducing the effect of the different shapes of electron-pair domains. However, the the-

TABLE V. Lattice constants, cohesive energies, elastic constants, ISFE, USFEs, cleavage energies, surface formation energies, and relative phase energies of $E_{\mathrm{hdia}} - E_{\mathrm{cdia}}$ for BN with hybrid potential alongside DFT data and other studies for comparison.

		Unit	DFT	Hybrid	Tersoff [98]	Tersoff [45]	Tersoff [42]
Cubic	a_0	Å	3.63[a]	3.63	3.49	3.63	3.62
BN	E_C	eV	6.59[a]	6.60	7.78	6.59	6.63
	C_{11}	GPa	790[a]	752	636	783	680
	C_{12}	GPa	217[a]	221	382	171	229
	C_{44}^0	GPa		313	593	446	516
	C_{44}	GPa	448[a]	308	346	358	405
	$\gamma_{\mathrm{USFE}}^{\{111\}[112]}$	J/m^2	3.76[b]	5.86	4.68	11.1	6.72
	$\gamma_{\mathrm{ISFE}}^{\{111\}[112]}$	J/m^2	0.19[b]	0.02	0.00	0.00	0.00
	$\gamma_{\mathrm{USFE}}^{\{111\}[110]}$	J/m^2	7.47[b]	8.08	4.83	8.21	7.52
	$\gamma_{\mathrm{USFE}}^{\{110\}[110]}$	J/m^2	9.01[c]	11.4	7.04	11.1	10.1
	$\gamma_{\mathrm{USFE}}^{\{100\}[110]}$	J/m^2	14.5[c]	13.5	7.39	13.0	10.9
	$E_b^{\{111\}}$	J/m^2	13.9[c]	11.2	7.74	9.26	7.42
	$\gamma^{\{111\}}$	J/m^2	6.05[c]	5.14	2.64	4.63	3.25
Hexagonal	a_0	Å	2.55[a]	2.57	2.14	2.56	2.56
BN	c_0	Å	4.23[a]	4.19	4.03	4.19	4.18
	$E_{\mathrm{hdia}} - E_{\mathrm{cdia}}$	meV	17[a]	1.1	0.0	0.0	0.0
	C_{11}	GPa	929[a]	790	785	847	849
	C_{12}	GPa	130[a]	203	318	142	181
	C_{13}	GPa	57[a]	192	266	136	109
	C_{33}	GPa	1013[a]	806	925	853	920
	C_{44}	GPa	329[a]	281	200	324	285

[a]Reference [78].

[b]Reference [113].

[c]DFT calculations in this work.

oretical basis of the two-center, orthogonal TB approximation that bonding exists only between the first-nearest neighbors (1NNs) within the molecule as the valence orbitals are tightly bound to their parent atoms [32] as well as the complexity and computational inefficiency limit its applicability for long-range effects, i.e., it is difficult to include more neighbor atoms beyond the second-nearest neighbors (2NNs). Such a deficiency may induce artifacts, such as the conflict between the sequence order of SFEs and cleavage energy for covalent

solids, absent interplanar interactions for graphite, and unreliable diamond-to-graphite transformation [43]. By combining the long-range functional term and the short-range angular-dependent term, the hybrid potential model could effectively balance their respective deficiencies while displaying their superiorities, particularly for the mixed bonding solids consisting of metallic and covalent elements.

The present hybrid potential model adopted a rough approximation (a zeroth-order approximation specifically) of
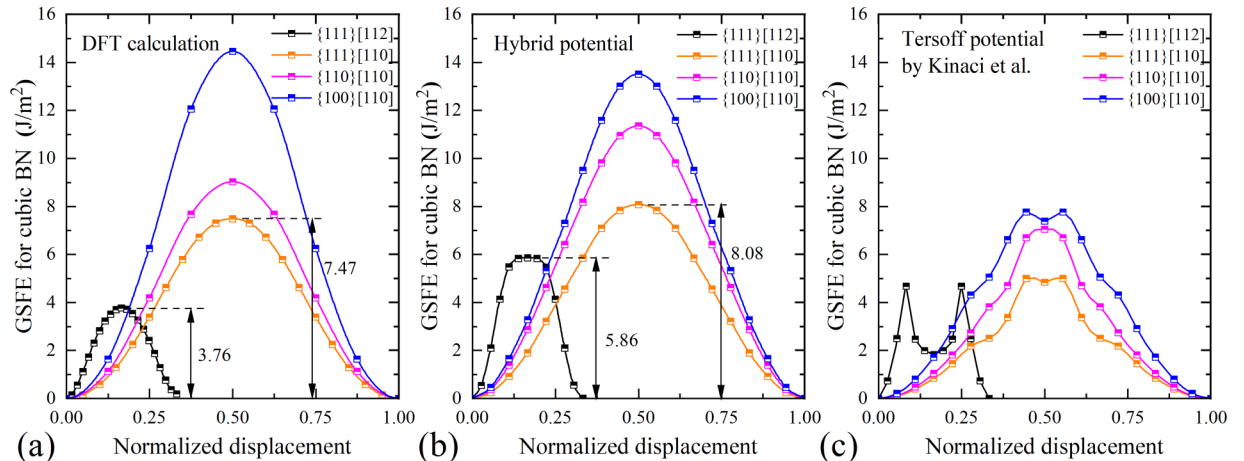
FIG. 8. GSFE curves along [112] direction on {111} planes and along [110] direction on {001}, {110}, and {111} planes of cubic BN with (a) DFT calculation, (b) hybrid potential, and (c) published Tersoff potential [98].

the local electron density as a linear superposition of spherically averaged electron densities from each neighbor atom. Nevertheless, it substantially reduced the computation cost, with the errors being compensated by the short-range angular-dependent term. It should be noted that one may introduce high-order corrections to the spherically averaged approximation by incorporating directional dependence in the electron density in a similar manner to the MEAM potential model, but it may reduce the computational efficiency in simulations. To demonstrate the efficiency of the hybrid potential model, Fig. S6 presents a comparison of the wall clock time during the uniaxial tension simulations of elemental crystals by using the hybrid potentials, previously published MEAM potentials, and constructed fictional potentials (see Supplemental Material for simulation details [67]; see also Refs. [3,39,40,42,45,55,59,75,77–97], therein). For metallic systems, the 1NN/2NN MEAM potential [55,111] and the hybrid potential with 2NN cutoff for the short-range term require more time than that required by the EAM [59] and FS potentials [79] because of the additional angular-dependent term. The time required by the hybrid potential (10.4 h) is roughly equivalent to the sum of the long-range pair-functional potential (1.77 h) and the 2NN MEAM potential (9.26 h). For covalent systems, the time required by the hybrid C potential (0.928 h) is between the values of Tersoff cluster potentials with 1NN [75] and 2NN (0.133 and 6.75 h, respectively) because its short-range term used only 1NN. In addition, as exhibited in Fig. S6(b), the increasing cutoff for the angular-dependent term will result in more computational demands; thus, it is much more efficient to add a long-range term in the hybrid potential model than to directly increase the cutoff in the cluster potential model to include the long-range interactions. In brief, although the hybrid potential demands some additional computational efforts, it might improve flexibility, compatibility, and accuracy to a certain degree.

By further demonstrating the capability of the hybrid potential model for compound systems consisting of both metallic and covalent elements, it can be observed that the elemental potentials may be seamlessly combined based on the scale-invariance rule without any reliability loss. By contrast, it is challenging to use the pair-functional potentials or cluster potentials in combining two elements with different bonding natures, e.g., the incompatibility between EAM and Tersoff potential, primarily due to the following reasons: (1) compatibility issues arising from nonuniform potential functional forms, (2) parameters with the order of magnitude different from various sources of elemental potentials, and (3) complexity originating from the multidimensional space of the fitting parameters for compound systems. By combining different types of potential models, the aforementioned difficulties could be readily resolved by the present hybrid potential model, providing the opportunity to perform simulations on systems consisting of different bonding elements

with high fidelity and feasibility. In brief, the high compatibility and transferability shown in the aforementioned cases validate the fidelity of the hybrid potential model for various simulation scenes.

V. CONCLUSIONS

In summary, by incorporating the long-range many-body effect into pair-functional potentials and the short-range angular-dependent terms into cluster potentials, a flexible and accurate hybrid potential is proposed in this paper. The main conclusions of this study can be summarized as follows:

(1) The hybrid potential had high compatibility for both metallic and covalent elements, which was demonstrated for 20 metals (including fcc, bcc, and hcp metals) and three covalent solids with reliable mechanical property reproduction.

(2) Several critical issues were resolved after combining the two physical ideas, including the incorrect phase stability for metals with high c/a ratios and the conflict between the correct sequence order of SFEs and cleavage energy for covalent solids.

(3) The unified expression in the hybrid potential facilitated the construction of the cross potential, which was extended to compounds by combining elemental potentials under the scale-invariance rule, such as BN, CuNi, and TiC, indicating its flexibility for alloy and compound simulations.

(4) Finally, the physical basis for the hybrid potential model has been justified: the basic idea of long-range many-body pair functional term comes from DFT that assumes each atom to be embedded in a host electron cloud as used in the EAM model, whereas the short-range angular-dependent correction is inspired by the VSEPR theory and TB theory to account for the localized covalent components by the electron-pair overlapping, as characterized in the Tersoff model.

Overall, the present hybrid potential model could provide an alternative to constructing high-feasibility potentials for both metallic and covalent solids with reasonable improvement in the pair-functional potential and cluster potential, thus laying a foundation for further potential development with broader applications.

[1] D. L. McDowell and S. R. Kalidindi, The materials innovation ecosystem: A key enabler for the Materials Genome Initiative, MRS Bull. **41**, 326 (2016).

[2] X. F. Kong, N. Gao, I. J. Beyerlein, B. N. Yao, S. J. Zheng, X. L. Ma, D. Legut, T. C. Germann, H. J. Zhang, and R. F. Zhang, Interface facilitated transformation of voids

directly into stacking fault tetrahedra, Acta Mater. **188**, 623 (2020).

[3] X. W. Zhou, R. A. Johnson, and H. N. G. Wadley, Misfit-energy-increasing dislocations in vapor-deposited CoFe/NiFe multilayers, Phys. Rev. B **69**, 144113 (2004).

[4] X. Y. Chen, X. F. Kong, A. Misra, D. Legut, B. N. Yao, T. C. Germann, and R. F. Zhang, Effect of dynamic evolution of misfit dislocation pattern on dislocation nucleation and shear sliding at semi-coherent bimetal interfaces, Acta Mater. **143**, 107 (2018).

[5] B. N. Yao, Z. R. Liu, D. Legut, X. F. Kong, T. C. Germann, H. J. Zhang, and R. F. Zhang, Cooperative roles of stacking fault energies on dislocation nucleation at bimetal interface through tunable potentials, Comput. Mater. Sci. **193**, 110416 (2021).

[6] X. F. Kong, I. J. Beyerlein, Z. R. Liu, B. N. Yao, D. Legut, T. C. Germann, and R. F. Zhang, Stronger and more failure-resistant with three-dimensional serrated bimetal interfaces, Acta Mater. **166**, 231 (2019).

[7] A. Ramasubramaniam, M. Itakura, and E. A. Carter, Inter-atomic potentials for hydrogen in α–iron based on density functional theory, Phys. Rev. B **79**, 174101 (2009).

[8] X. P. Shen, B. N. Yao, Z. R. Liu, D. Legut, H. J. Zhang, and R. F. Zhang, Mechanistic insights into interface-facilitated dislocation nucleation and phase transformation at semicoherent bimetal interfaces, Int. J. Plast. **146**, 103105 (2021).

[9] D. G. Pettifor and I. I. Oleynik, Interatomic bond-order potentials and structural prediction, Prog. Mater Sci. **49**, 285 (2004).

[10] G. Mie, Kinetic theory of monatomic bodies, Ann. Phys **316**, 657 (1903).

[11] J. E. Lennard-Jones, On the forces between atoms and ions, Proc. R. Soc. London, Ser. A **109**, 584 (1925).

[12] P. M. Morse, Diatomic molecules according to the wave mechanics. II. Vibrational levels, Phys. Rev. **34**, 57 (1929).

[13] M. Born and J. E. Mayer, Zur gittertheorie der ionenkristalle, Z. Angew. Phys. **75**, 1 (1932).

[14] J. H. Li, Y. Dai, and X. D. Dai, Long-range n-body potential and applied to atomistic modeling the formation of ternary metallic glasses, Intermetallics **31**, 292 (2012).

[15] F. H. Stillinger and T. A. Weber, Computer simulation of local order in condensed phases of silicon, Phys. Rev. B **31**, 5262 (1985).

[16] M. S. Daw and M. I. Baskes, Embedded-atom method: Derivation and application to impurities, surfaces, and other defects in metals, Phys. Rev. B **29**, 6443 (1984).

[17] D. Tománek, A. A. Aligia, and C. A. Balseiro, Calculation of elastic strain and electronic effects on surface segregation, Phys. Rev. B **32**, 5051 (1985).

[18] G. J. Ackland, M. W. Finnis, and V. Vitek, Validity of the second moment tight-binding model, J. Phys. F: Met. Phys. **18**, L153 (1988).

[19] M. W. Finnis and J. E. Sinclair, A simple empirical N-body potential for transition metals, Philos. Mag. A **50**, 45 (1984).

[20] J. Tersoff, Empirical interatomic potential for silicon with improved elastic properties, Phys. Rev. B **38**, 9902 (1988).

[21] J. Tersoff, New empirical approach for the structure and energy of covalent systems, Phys. Rev. B **37**, 6991 (1988).

[22] J. Tersoff, Carbon Defects and Defect Reactions in Silicon, Phys. Rev. Lett. **64**, 1757 (1990).

[23] D. W. Brenner, Empirical potential for hydrocarbons for use in simulating the chemical vapor deposition of diamond films, Phys. Rev. B **42**, 9458 (1990).

[24] S. M. Foiles, Calculation of the surface segregation of Ni-Cu alloys with the use of the embedded-atom method, Phys. Rev. B **32**, 7685 (1985).

[25] S. M. Foiles, M. I. Baskes, and M. S. Daw, Embedded-atom-method functions for the fcc metals Cu, Ag, Au, Ni, Pd, Pt, and their alloys, Phys. Rev. B **33**, 7983 (1986).

[26] F. Ducastelle and F. Cyrot-Lackmann, Moments developments and their application to the electronic charge distribution of d bands, J. Phys. Chem. Solids **31**, 1295 (1970).

[27] X. D. Dai, Y. Kong, and J. H. Li, Long-range empirical potential model: Application to fcc transition metals and alloys, Phys. Rev. B **75**, 104101 (2007).

[28] X. D. Dai, J. H. Li, and Y. Kong, Long-range empirical potential for the bcc structured transition metals, Phys. Rev. B **75**, 052102 (2007).

[29] D. Choudhuri, S. G. Srinivasan, and R. S. Mishra, Deformation of lamellar FCC-B2 nanostructures containing Kurdjumov-Sachs interfaces: Relation between interfacial structure and plasticity, Int. J. Plast. **125**, 191 (2020).

[30] R. F. Zhang, I. J. Beyerlein, S. J. Zheng, S. H. Zhang, A. Stukowski, and T. C. Germann, Manipulating dislocation nucleation and shear resistance of bimetal interfaces by atomic steps, Acta Mater. **113**, 194 (2016).

[31] Z. R. Liu, B. N. Yao, D. Legut, X. F. Kong, T. C. Germann, H. J. Zhang, and R. F. Zhang, Mechanistic understanding of the size effect on shock facilitated dislocation nucleation at semicoherent interfaces, Scr. Mater. **178**, 457 (2020).

[32] D. G. Pettifor, *Bonding and Structure of Molecules and Solids* (Oxford University Press, Oxford, 1995).

[33] S. Starikov, D. Smirnova, T. Pradhan, Y. Lysogorskiy, H. Chapman, M. Mrovec, and R. Drautz, Angular-dependent interatomic potential for large-scale atomistic simulation of iron: Development and comprehensive comparison with existing interatomic models, Phys. Rev. Mater. **5**, 063607 (2021).

[34] Y. Mishin, M. J. Mehl, and D. A. Papaconstantopoulos, Phase stability in the Fe–Ni system: Investigation by first-principles calculations and atomistic simulations, Acta Mater. **53**, 4029 (2005).

[35] S. Starikov, D. Smirnova, T. Pradhan, I. Gordeev, R. Drautz, and M. Mrovec, Angular-dependent interatomic potential for large-scale atomistic simulation of the Fe-Cr-H ternary system, Phys. Rev. Mater. **6**, 043604 (2022).

[36] J. S. Gibson, S. G. Srinivasan, M. I. Baskes, R. E. Miller, and A. K. Wilson, A multi-state modified embedded atom method potential for titanium, Modell. Simul. Mater. Sci. Eng. **25**, 015010 (2016).

[37] P. Erhart, N. Juslin, O. Goy, K. Nordlund, R. Müller, and K. Albe, Analytic bond-order potential for atomistic simulations of zinc oxide, J. Phys.: Condens. Matter **18**, 6585 (2006).

[38] H. S. Jang, K. M. Kim, and B. J. Lee, Modified embedded-atom method interatomic potentials for pure Zn and Mg-Zn binary system, Calphad **60**, 200 (2018).

[39] G. Plummer, H. Rathod, A. Srivastava, M. Radovic, T. Ouisse, M. Yildizhan, P. O. Å. Persson, K. Lambrinou, M. W. Barsoum, and G. J. Tucker, On the origin of kinking in layered crystalline solids, Mater. Today **43**, 45 (2021).

[40] G. Plummer and G. J. Tucker, Bond-order potentials for the Ti$_3$AlC$_2$ and Ti$_3$SiC$_2$ MAX phases, Phys. Rev. B **100**, 214114 (2019).

[41] M. S. Daw, J. W. Lawson, and C. W. Bauschlicher, Interatomic potentials for Zirconium Diboride and Hafnium Diboride, Compr. Mater. Sci. **50**, 2828 (2011).

[42] C. Huang, B. Yang, X. Peng, and S. Chen, plastic deformation and hardening mechanisms of a nano-twinned cubic boron nitride ceramic, ACS Appl. Mater. Interfaces **12**, 50161 (2020).

[43] J. H. Los and A. Fasolino, Intrinsic long-range bond-order potential for carbon: Performance in Monte Carlo simulations of graphitization, Phys. Rev. B **68**, 024107 (2003).

[44] G. J. Ackland, Interatomic potential development, Compr. Nucl. Mater. 267 (2012).

[45] B. N. Yao, Z. R. Liu, and R. F. Zhang, EAPOTc: An integrated empirical interatomic potential optimization platform for compound solids, Comput. Mater. Sci. **211**, 111551 (2022).

[46] M. I. Baskes and R. A. Johnson, Modified embedded atom potentials for HCP metals, Modell. Simul. Mater. Sci. Eng. **2**, 147 (1994).

[47] M. I. Baskes, Commentary on 'modified embedded atom method potentials for hcp metals' MI Baskes and RA Johnson (1994) Modelling Simul. Mater. Sci. Eng.—the early basis for modeling hcp materials using MEAM, Modell. Simul. Mater. Sci. Eng. **25**, 071002 (2017).

[48] D. E. Dickel, M. I. Baskes, I. Aslam, and C. D. Barrett, New interatomic potential for Mg–Al–Zn alloys with specific application to dilute Mg-based alloys, Modell. Simul. Mater. Sci. Eng. **26**, 045010 (2018).

[49] S. Plimpton, Fast parallel algorithms for short-range molecular dynamics, J. Comput. Phys. **117**, 1 (1995).

[50] Z. R. Liu, B. N. Yao, and R. F. Zhang, SPaMD studio: An integrated platform for atomistic modeling, simulation, analysis, and visualization, Comput. Mater. Sci. **210**, 111027 (2022).

[51] R. A. Johnson, Analytic nearest-neighbor model for fcc metals, Phys. Rev. B **37**, 3924 (1988).

[52] A. Banerjea and J. R. Smith, Origins of the universal binding-energy relation, Phys. Rev. B **37**, 6632 (1988).

[53] R. A. Johnson and D. J. Oh, Analytic embedded atom method model for bcc metals, J. Mater. Res. **4**, 1195 (1989).

[54] X. W. Zhou, J. A. Zimmerman, B. M. Wong, and J. J. Hoyt, An embedded-atom method interatomic potential for Pd–H alloys, J. Mater. Res. **23**, 704 (2008).

[55] M. I. Baskes, Modified embedded-atom potentials for cubic materials and impurities, Phys. Rev. B **46**, 2727 (1992).

[56] I. Hijazi, Y. Zhang, and R. Fuller, A simple embedded atom potential for Pd-H alloys, Mol. Simul. **44**, 1371 (2018).

[57] L. M. Hale, B. M. Wong, J. A. Zimmerman, and X. W. Zhou, Atomistic potentials for palladium–silver hydrides, Modell. Simul. Mater. Sci. Eng. **21**, 045005 (2013).

[58] J. Tersoff, Modeling solid-state chemistry: Interatomic potentials for multicomponent systems, Phys. Rev. B **39**, 5566 (1989).

[59] B. Onat and S. Durukanoğlu, An optimized interatomic potential for Cu–Ni alloys with the embedded-atom method, J. Phys.: Condens. Matter **26**, 035404 (2013).

[60] M. J. Demkowicz and R. G. Hoagland, Structure of Kurdjumov–Sachs interfaces in simulations of a copper–niobium bilayer, J. Nucl. Mater. **372**, 45 (2008).

[61] B. N. Yao, Z. R. Liu, and R. F. Zhang, EAPOTs: An integrated empirical interatomic potential optimization platform for single elemental solids, Comput. Mater. Sci. **197**, 110626 (2021).

[62] C. Jeffrey, James Lagarias, Reeds A, H. Margaret, Wright, and Paul, Convergence properties of the Nelder–Mead simplex method in low dimensions, SIAM J. Optim. **9**, 112 (1998).

[63] M. J. Demkowicz and R. G. Hoagland, Simulations of collision cascades in Cu–Nb layered composites using an eam interatomic potential, Int. J. Appl. Mech. **1**, 421 (2009).

[64] M. I. Mendelev and G. J. Ackland, Development of an interatomic potential for the simulation of phase transformations in zirconium, Philos. Mag. Lett. **87**, 349 (2007).

[65] Y. Mishin, D. Farkas, M. J. Mehl, and D. A. Papaconstantopoulos, Interatomic potentials for monoatomic metals from experimental data and ab initio calculations, Phys. Rev. B **59**, 3393 (1999).

[66] Y. Mishin, M. J. Mehl, D. A. Papaconstantopoulos, A. F. Voter, and J. D. Kress, Structural stability and lattice defects in copper: Ab initio, tight-binding, and embedded-atom calculations, Phys. Rev. B **63**, 224106 (2001).

[67] See Supplemental Material at http://link.aps.org/supplemental/10.1103/PhysRevB.108.024108 for additional details of embedded-atom method and potential fitting procedure. Supplemental Material also includes Refs. [3,39,40,42,45,55,59,75,77–97].

[68] P. L. Williams, Y. Mishin, and J. C. Hamilton, An embedded-atom potential for the Cu–Ag system, Modell. Simul. Mater. Sci. Eng. **14**, 817 (2006).

[69] H. W. Sheng, M. J. Kramer, A. Cadien, T. Fujita, and M. W. Chen, Highly optimized embedded-atom-method potentials for fourteen fcc metals, Phys. Rev. B **83**, 134118 (2011).

[70] https://sites.google.com/site/eampotentials/ (accessed 1 Oct. 2022).

[71] M. Igarashi, M. Khantha, and V. Vitek, N-body interatomic potentials for hexagonal close-packed metals, Philos. Mag. B **63**, 603 (1991).

[72] D. K. Ward, X. W. Zhou, B. M. Wong, F. P. Doty, and J. A. Zimmerman, Analytical bond-order potential for the Cd-Zn-Te ternary system, Phys. Rev. B **86**, 245203 (2012).

[73] U. Wedig, M. Jansen, B. Paulus, K. Rosciszewski, and P. Sony, Structural and electronic properties of Mg, Zn, and Cd from Hartree-Fock and density functional calculations including hybrid functionals, Phys. Rev. B **75**, 205123 (2007).

[74] N. Gaston, B. Paulus, U. Wedig, and M. Jansen, Multiple Minima on the Energy Landscape of Elemental Zinc: A Wave Function Based Ab Initio Study, Phys. Rev. Lett. **100**, 226404 (2008).

[75] J. Tersoff, Chemical order in amorphous silicon carbide, Phys. Rev. B **49**, 16349 (1994).

[76] S. J. Mahdizadeh and G. Akhlamadi, Optimized Tersoff empirical potential for germanene, J. Mol. Graph. Modell. **72**, 1 (2017).

[77] A. I. Gusev, Phase equilibria, phases and compounds in the Ti–C system, Russ. Chem. Rev. **71**, 439 (2002).

[78] A. Jain, S. P. Ong, G. Hautier, W. Chen, W. D. Richards, S. Dacek, S. Cholia, D. Gunter, D. Skinner, and G. Ceder, Commentary: The Materials Project: A materials genome approach to accelerating materials innovation, APL Mater. **1**, 011002 (2013).

[79] M. I. Mendelev, M. J. Kramer, C. A. Becker, and M. Asta, Analysis of semi-empirical interatomic potentials appropriate for simulation of crystalline and liquid Al and Cu, Philos. Mag. **88**, 1723 (2008).

[80] X. Z. Wu, R. Wang, S. F. Wang, and Q. Y. Wei, Ab initio calculations of generalized-stacking-fault energy surfaces and surface energies for FCC metals, Appl. Surf. Sci. **256**, 6345 (2010).

[81] J. A. Zimmerman, H. Gao, and F. F. Abraham, Generalized stacking fault energies for embedded atom FCC metals, Modell. Simul. Mater. Sci. Eng. **8**, 103 (2000).

[82] S. L. Shang, B. C. Zhou, W. Y. Wang, A. J. Ross, X. L. Liu, Y. J. Hu, H. Z. Fang, Y. Wang, and Z. K. Liu, A comprehensive first-principles study of pure elements: Vacancy formation and migration energies and self-diffusion coefficients, Acta Mater. **109**, 128 (2016).

[83] R. F. Zhang, S. H. Zhang, Z. J. He, J. Jing, and S. H. Sheng, Miedema Calculator: A thermodynamic platform for predicting formation enthalpies of alloys within framework of Miedema's Theory, Comput. Phys. Commun. **209**, 58 (2016).

[84] R. Tran, Z. Xu, B. Radhakrishnan, D. Winston, W. Sun, K. A. Persson, and S. P. Ong, Surface energies of elemental crystals, Sci. Data **3**, 160080 (2016).

[85] S. L. Shang, A. Saengdeejing, Z. G. Mei, D. E. Kim, H. Zhang, S. Ganeshan, Y. Wang, and Z. K. Liu, First-principles calculations of pure elements: Equations of state and elastic stiffness constants, Comput. Mater. Sci. **48**, 813 (2010).

[86] Q. M. Hu and R. Yang, Basal-plane stacking fault energy of hexagonal close-packed metals based on the Ising model, Acta Mater. **61**, 1136 (2013).

[87] X. Wu, R. Wang, and S. Wang, Generalized-stacking-fault energy and surface properties for HCP metals: A first-principles study, Appl. Surf. Sci. **256**, 3409 (2010).

[88] A. F. Voter and S. P. Chen, Characterization of defects in materials, Mater. Res. Soc. Symp. Proc. **82**, 175 (1987).

[89] Y. M. Kim and B. J. Lee, Modified embedded-atom method interatomic potentials for the Ti–C and Ti–N binary systems, Acta Mater. **56**, 3481 (2008).

[90] R. Ahuja, O. Eriksson, J. M. Wills, and B. Johansson, Structural, elastic, and high-pressure properties of cubic TiC, TiN, and TiO, Phys. Rev. B **53**, 3072 (1996).

[91] A. Stukowski and K. Albe, Extracting dislocations and non-dislocation crystal defects from atomistic simulation data, Modell. Simul. Mater. Sci. Eng. **18**, 085001 (2010).

[92] A. Stukowski, V. V. Bulatov, and A. Arsenlis, Automated identification and indexing of dislocations in crystal interfaces, Modell. Simul. Mater. Sci. Eng. **20**, 085007 (2012).

[93] A. Stukowski, Visualization and analysis of atomistic simulation data with OVITO–the Open Visualization Tool, Modell. Simul. Mater. Sci. Eng. **18**, 015012 (2009).

[94] V. L. Moruzzi, J. F. Janak, and K. Schwarz, Calculated thermal properties of metals, Phys. Rev. B **37**, 790 (1988).

[95] M. Körling and J. Häglund, Cohesive and electronic properties of transition metals: The generalized gradient approximation, Phys. Rev. B **45**, 13293 (1992).

[96] L. Malerba, M. C. Marinica, N. Anento, C. Björkas, H. Nguyen, C. Domain, F. Djurabekova, P. Olsson, K. Nordlund, and A. Serra, Comparison of empirical interatomic potentials for iron applied to radiation damage studies, J. Nucl. Mater. **406**, 19 (2010).

[97] M. R. Fellinger, Ph.D. thesis, The Ohio State University, 2013.

[98] A. Kınacı, J. B. Haskins, C. Sevik, and T. Çağın, Thermal conductivity of BN-C nanostructures, Phys. Rev. B **86**, 115410 (2012).

[99] S. H. Zhang, X. Zheng, Q. Q. Jin, S. J. Zheng, D. Legut, X. H. Yu, H. Y. Gou, Z. H. Fu, Y. Q. Guo, and B. M. Yan, Unprecedented plastic flow channel in γ-B28 through ultrasoft bonds: A challenge to superhardness, Phys. Rev. Mater. **2**, 123602 (2018).

[100] A. Nie, Y. Bu, J. Huang, Y. Shao, Y. Zhang, W. Hu, J. Liu, Y. Wang, B. Xu, Z. Liu, H. Wang, W. Yang, and Y. Tian, Direct observation of room-temperature dislocation plasticity in diamond, Matter **2**, 1222 (2020).

[101] M. S. Daw and M. I. Baskes, Semiempirical, Quantum Mechanical Calculation of Hydrogen Embrittlement in Metals, Phys. Rev. Lett. **50**, 1285 (1983).

[102] P. Hohenberg and W. Kohn, Density functional theory (DFT), Phys. Rev **136**, B864 (1964).

[103] M. J. Stott and E. Zaremba, Quasiatoms: An approach to atoms in nonuniform electronic systems, Phys. Rev. B **22**, 1564 (1980).

[104] C. Kittel, P. McEuen, and P. McEuen, *Introduction to Solid State Physics* (Wiley, New York, 1996), Vol. 8.

[105] J. M. Rowe, B. N. Brockhouse, and E. C. Svensson, Lattice Dynamics of White Tin, Phys. Rev. Lett. **14**, 554 (1965).

[106] R. J. Gillespie and I. Hargittai, *The VSEPR Model of Molecular Geometry* (Courier Corporation, North Chelmsford, 2013).

[107] I. I. Oleinik and D. G. Pettifor, Analytic bond-order potentials beyond Tersoff-Brenner. II. Application to the hydrocarbons, Phys. Rev. B **59**, 8500 (1999).

[108] D. G. Pettifor and I. I. Oleinik, Analytic bond-order potentials beyond Tersoff-Brenner. I. Theory, Phys. Rev. B **59**, 8487 (1999).

[109] D. G. Pettifor and I. I. Oleinik, Bounded Analytic Bond-Order Potentials for Σ and Π Bonds, Phys. Rev. Lett. **84**, 4124 (2000).

[110] A. P. Horsfield, A. M. Bratkovsky, M. Fearn, D. G. Pettifor, and M. Aoki, Bond-order potentials: Theory and implementation, Phys. Rev. B **53**, 12694 (1996).

[111] A. Agrawal and R. Mirzaeifar, Copper-graphene composites; developing the MEAM potential and investigating their mechanical properties, Comput. Mater. Sci. **188**, 110204 (2021).

[112] E. Grüneisen and E. Goens, Researches on metal crystals. i. elastic constants of zinc and cadmium, Z. für Phys. **26**, 235 (1924).

[113] T. Xu, S. Zhang, D. Legut, S. Veprek, and R. Zhang, Revealing the pressure-induced softening/weakening mechanism in representative covalent materials, Chin. Phys. Lett. **38**, 056101 (2021).